

Band gap and electronic structure of cubic, rhombohedral, and orthorhombic In_2O_3 polymorphs: Experiment and theory

T. de Boer,^{1,*} M. F. Bekheet,² A. Gurlo,² R. Riedel,³ and A. Moewes¹¹*Department of Physics and Engineering Physics, University of Saskatchewan, 116 Science Place, Saskatoon, Saskatchewan, Canada S7N 5E2*²*Fachgebiet Keramische Werkstoffe, Institut für Werkstoffwissenschaften und -technologien, Technische Universität Berlin, Hardenbergstraße 40, 10623 Berlin, Germany*³*Fachbereich Material- und Geowissenschaften, Fachgebiet Disperse Feststoffe, Jovank-Bontschits-Strasse 2, 64287 Darmstadt, Germany*

(Received 7 August 2015; revised manuscript received 30 March 2016; published 18 April 2016)

Recent studies on In_2O_3 have revealed a rich phase diagram and have led to the discovery of new In_2O_3 polymorphs, including the synthesis and ambient recovery of $Pbcn$ In_2O_3 . The electronic properties of this new phase are studied together with other better-known polymorphs ($Ia\bar{3}$ and $R\bar{3}c$) using soft x-ray absorption and emission spectroscopy, directly probing the partial density of states and transition matrix elements. Together with complementary full-potential all-electron density functional theory calculations, this allows important material parameters, such as the electronic band gap and partial density of states, to be elucidated. Excellent agreement between experiment and theory is obtained, with band gaps of 3.2 ± 0.3 , 3.1 ± 0.3 , and 2.9 ± 0.3 eV determined for the $Ia\bar{3}$, $R\bar{3}c$, and $Pbcn$ In_2O_3 polymorphs, respectively. The effective mass of carriers in $Pbcn$ In_2O_3 is predicted to be 12% less than in the widely used $Ia\bar{3}$ polymorph while having a similar effective optical band gap.

DOI: [10.1103/PhysRevB.93.155205](https://doi.org/10.1103/PhysRevB.93.155205)

I. INTRODUCTION

Indium oxide (In_2O_3) is a transparent semiconducting oxide which can become conducting if grown in oxygen-poor environments or doped with atoms such as Sn [1]. In this case, the combination of transparency at optical wavelengths, reflectivity at infrared wavelengths [2], and high conductivity has facilitated the use of In_2O_3 as a transparent conductive layer in a broad range of applications, including in solar cells [1,3], light-emitting diodes [4,5], and liquid-crystal displays [6], as well as a cladding layer in GaN-based laser diodes [7,8]. In_2O_3 is also used in gas-sensing applications owing to the sensitivity of electrical properties such as conductivity and the Seebeck coefficient to the local environment [1,9–14].

The multitude of applications of In_2O_3 has recently lead to extensive studies exploring the phase diagram of this material as new polymorphs may have more favorable properties or open up new applications [15–20]. The existence of a high-pressure rhombohedral corundum-type polymorph of In_2O_3 has long been known [21] and has recently attracted interest due to advances in the synthesis of this material [17,22–25]. This polymorph exhibits more stable conductivity than the widely used cubic polymorph [26] and has been found to be useful in gas-sensing applications, being highly sensitive to dilute ethanol, H_2S , and ammonia [27,28]. It has also been tested as an anode material for lithium-ion batteries and showed an enhanced and stable capacity compared to the commonly used cubic polymorph [29]. In environmental applications, it has been reported to exhibit excellent photocatalytic activities for degenerating rhodamine B and methylene blue dyes under UV irradiation [30]. Recently, new metastable phases such as orthorhombic $Pbcn$ [19,31] and $Pbca$ [20] In_2O_3 have been synthesized, although only $Pbcn$ In_2O_3 has been recovered

at ambient conditions. The properties of $Pbcn$ In_2O_3 are not known since this polymorph was not available at ambient pressure before this work.

To facilitate the use of new In_2O_3 polymorphs in applications, a detailed understanding of their electronic structure is required. In this work cubic bixbyite ($Ia\bar{3}$, no. 206), rhombohedral corundum-type ($R\bar{3}c$, no. 167), and orthorhombic ($Pbcn$, no. 60) In_2O_3 , henceforth referred to as c- In_2O_3 , rh- In_2O_3 , and o- In_2O_3 , respectively, are studied using soft x-ray absorption spectroscopy (XAS) and soft x-ray emission spectroscopy (XES). These measurements, which directly probe the partial electronic density of states and transition matrix elements of a material, are compared with theoretical spectra calculated using density functional theory, providing support for the calculated electronic properties.

II. EXPERIMENTAL AND CALCULATION DETAILS

A. Sample synthesis

High-purity (99.999%) c- In_2O_3 was obtained commercially from Sigma-Aldrich. Rh- In_2O_3 and o- In_2O_3 samples were also studied. Rh- In_2O_3 was synthesized by precipitation from the solution of indium nitrate in methanol by adding a concentrated ammonia solution and subsequent calcination of the obtained precipitate at 500 °C [23]. The orthorhombic o- In_2O_3 was obtained from the rh- In_2O_3 polymorph under high-pressure, high-temperature conditions (8–9 GPa, 600–1100°C) in a multianvil and toroid apparatus [19]. The synthesis of o- In_2O_3 as well as the structural parameters of both rh- In_2O_3 and o- In_2O_3 are described in detail elsewhere [19].

B. XAS and XES measurements

X-ray absorption and emission spectroscopy, which are sensitive to the unoccupied and occupied partial density of states (PDOS) of a particular element, respectively, were per-

*tristan.deboer@usask.ca

formed at the O $1s$ and O K_{α} edges of each In_2O_3 polymorph. XES measurements with excitation energies far above the excitation threshold were performed at beamline 8.0.1 of the Advanced Light Source (ALS) at Lawrence Berkeley National Laboratory, while XAS and resonant inelastic x-ray scattering (RIXS) measurements were performed at the REIXS beamline of the Canadian Light Source (CLS). These measurements are performed by promoting core electrons to the conduction band and monitoring their scattering (RIXS) or subsequent decay (XAS, XES). The resolving powers $E/\Delta E$ of the XAS and XES measurements at the CLS are 5000 and 600, respectively, while the resolving power of XES measurements at the ALS is 800. Samples were pressed onto carbon tape, and XAS measurements were performed in total electron yield (TEY) and total fluorescence yield (TFY) modes. All measurements were performed with the sample mounted 45° to the incident beam. XES spectra were collected using a soft x-ray fluorescence spectrometer in a Rowland circle geometry oriented at 90° with respect to the incident radiation. The measured spectra were calibrated using a powder bismuth germanate (BGO) sample. The XAS spectra were calibrated using an initial peak of 532.7 eV, while the XES spectra were calibrated using BGO features located at 517.9 and 526.0 eV. All measurements were performed at room temperature.

C. Calculation details

The electronic structure of the In_2O_3 polymorphs was modeled using density functional theory (DFT) with WIEN2K (version 13.1), a full-potential all-electron commercially available software package which uses linearized augmented plane waves with local orbitals in a Kohn-Sham scheme [32]. Calculations were performed using the Perdew, Burke, and Ernzerhof generalized gradient approximation (PBE-GGA) exchange-correlation functional. Since the PBE-GGA generally significantly underestimates the band gap of materials, the modified Becke-Johnson (mBJ) exchange-correlation functional is also used [33].

Calculations were performed using experimental lattice parameters, and to investigate the effect of strain present in the experimental structures, calculations in which the atomic positions and lattice parameters were allowed to relax were also performed. Since it is well known that the PBE-GGA functional tends to overestimate the lattice parameters of semiconductors, changes in relaxed unit-cell volume were also investigated using a formulation of the generalized gradient approximation which yields improved equilibrium lattice constants (PBEsol) [34], as well as using the local-density approximation (LDA) [35], which tends to underestimate lattice parameters. The experimental and calculated relaxed crystal structure parameters used in this study are shown in Table I. In all calculations $RK_{\max} = 7$ was used, and the k mesh was selected so that the total energy per unit cell was stable to within 10^{-5} Ry. This resulted in $10 \times 10 \times 10$, $21 \times 21 \times 21$, and $13 \times 19 \times 19$ k meshes for the c- In_2O_3 , rh- In_2O_3 , and o- In_2O_3 polymorphs, respectively.

The DFT calculations are used to calculate the density of states and band structure, as well as to directly calculate predicted XES and XAS spectra, allowing for a detailed comparison with experiment. The spectra are calculated by

multiplying the PDOS with a dipole transition matrix and a radial transition probability [36]. The calculated spectra are broadened using a combination of Lorentzian and Gaussian line shapes reflecting lifetime and instrumentation-related broadening, respectively. The XAS and XES spectra depend on the final state of the system for that measurement, which for XAS spectra corresponds to a crystal perturbed by the presence of a core hole [37,38], which tends to shift spectral weight to lower energies. To account for this perturbation, a core hole was added to a single atom in a supercell of each In_2O_3 polymorph such that individual core holes would be separated by at least 10 \AA , and separate core-hole calculations were performed for each oxygen atomic site. This resulted in $1 \times 1 \times 1$, $2 \times 2 \times 2$, and $2 \times 2 \times 2$ supercells for c- In_2O_3 , rh- In_2O_3 , and o- In_2O_3 , respectively, with correspondingly smaller k meshes.

III. RESULTS AND DISCUSSION

A. Agreement between experiment and theory

The measured XES and XAS spectra for each In_2O_3 polymorph are shown in Fig. 1 together with spectra calculated using the PBE-GGA functional. The calculated spectra in the presence and absence of a core hole are shown with solid and short dotted lines, respectively. Calculated spectra corresponding to the experimental structures are shown in blue and magenta, while spectra corresponding to a lattice with relaxed atomic positions are shown in orange.

Considering the XAS, the overall agreement between the measured and calculated experimental spectra is excellent, with all major features reproduced at approximately the correct energy position and at the correct peak intensity with the exception of feature b in the rh- In_2O_3 spectra. The TEY and TFY spectra, which are relatively surface and bulk sensitive, respectively, are in excellent agreement, suggesting that the measured spectra are representative of the bulk material and no surface contaminants are present. As previously noted, the PBE-GGA functional tends to underestimate the band gap of semiconductors, so the calculated spectra have been rigidly shifted to align spectral features.

Performing calculations in which the atomic positions are allowed to relax yields differences of less than 0.01 \AA for the c- In_2O_3 and rh- In_2O_3 polymorphs, resulting in negligible differences between the calculated XES and XAS spectra for the relaxed and experimental structures, shown in orange in Fig. 1. For o- In_2O_3 , the atomic positions shifted by at most 0.05 \AA , a considerably larger shift (with a similar change in nearest-neighbor distances). A corresponding larger difference between the calculated spectra for this polymorph is observed, with worse agreement with the experimentally measured spectra when the atoms are allowed to relax (particularly at features b, c, and d). This worse agreement (i) supports the experimentally determined structure parameters and (ii) suggests that the o- In_2O_3 phase is under internal strain, having been synthesized at high pressures, while the experiment is performed at ambient conditions and is thus far from equilibrium.

The metastability of the rh- and o- In_2O_3 polymorphs is further reflected in the calculated total energy, which increases

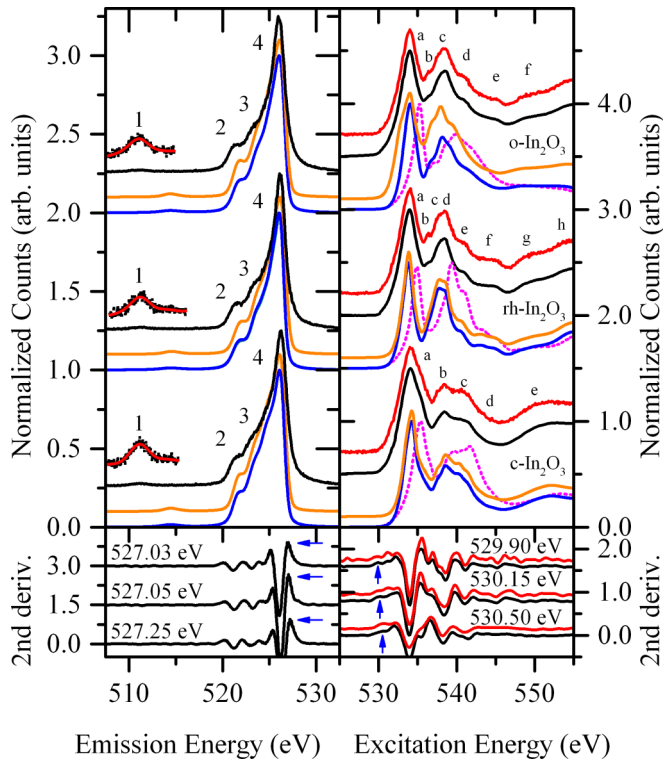


FIG. 1. (top left) Calculated and experimental O K XES spectra with excitation energy far above excitation threshold, with features labeled 1–4. Inset is a 10 \times magnification of feature 1 with a red line to guide the eye. Calculated spectra using the experimental atomic positions are shown in blue, with relaxed atomic positions in orange. (top right) Experimental TFY (TEY) XAS spectra are shown by red (black) lines. Calculated O K XAS spectra using experimental lattice structure are shown in the ground state (magenta dashed line) and with a core hole present (blue line). Calculated spectra for unit cells with relaxed atomic positions are shown in orange. (bottom) The second derivative of XES and XAS spectra, with peaks corresponding to band edges indicated by arrows with the peak energy shown in the diagram. The line color matches that of the underlying data. For each panel the data are presented for c-In $_2$ O $_3$, rh-In $_2$ O $_3$, and o-In $_2$ O $_3$ in ascending order.

as the density of the polymorph increases (shown in Table I). To assess the presence of compressive strain, the lattice parameters were allowed to relax, with fractional changes in unit-cell volume relative to known experimental values reported in Table I. It is well known that the PBE-GGA functional used in this study tends to overestimate lattice-cell parameters [34], so to assess any trends in relaxed volume as a function of input polymorph, the PBEsol and LDA functionals were also used. The results show that regardless of the type of functional used, the relaxed fractional unit-cell volume increases as the polymorph density increases. This increasing error with polymorph density reflects the overall compressive strain of the metastable rh-In $_2$ O $_3$ and o-In $_2$ O $_3$ polymorphs.

The XES spectra for each polymorph show four features (1–4) which are in excellent agreement with theory, with the exception of feature 1, which is misplaced by 3.2 eV. The disagreement between experiment and theory can be explained by considering the calculated density of states (DOS) in Fig. 2, which will be discussed in more detail below. It is well known that properly describing on-site Coulomb interaction in systems with relatively localized orbitals, such as In $4d$, is a shortcoming of the current level of theory. For each In $_2$ O $_3$ polymorph, the middle valence band (VB) is dominated by In d states which are hybridized with a small quantity of O p states. Studies on c-In $_2$ O $_3$ accounting for on-site self-interaction corrections (SICs) [40] or using functionals with a greater degree of chemical accuracy [41] confirm that although the spectral weight distribution of the In d states is incorrect at the current level of theory, the spectral weight in the uppermost VB is nevertheless well described. As such, the overall agreement for the main emission spectrum (features 2–4) provides experimental support for the calculated DOS for the uppermost VB, to which In d states make only a minor contribution. The incorrect positioning of feature 1, which is due to In d and O p hybridization, provides confirmation that only the calculated DOS of the uppermost VB in the current work is expected to be of physical significance and that the calculated energetic position of the second VB is incorrect. The position of feature 1 is the same for each polymorph and is in general agreement with prior measure-

TABLE I. Experimental (relaxed) lattice parameters for each In $_2$ O $_3$ polymorph together with the calculated total energy per formula unit. Fractional changes in the volume between the relaxed and experimental parameters are given by Δvol for the PBE-GGA, PBEsol (square brackets), and LDA functionals (curly brackets). Experimental parameters are taken from Ref. [39] for c-In $_2$ O $_3$ and Ref. [19] for rh-In $_2$ O $_3$ and o-In $_2$ O $_3$.

Compound and space group	Unit cell (\AA)	Atom	Wyckoff site	Wyckoff			Total energy per f.u. (Ry)
				x	y	z	
c-In $_2$ O $_3$ $Ia\bar{3}$	$a = 10.1170$ (10.2835)	In1	8b	0.25000 (0.25000)	0.25000 (0.25000)	0.25000 (0.25000)	-23984.8766
	$a = 10.1170$ (10.2835)	In2	24d	0.46650 (0.46591)	0.0000 (0.0000)	0.25000 (0.25000)	(-23984.8830)
	$a = 10.1170$ (10.2835)	O	48e	0.39085 (0.39094)	0.15435 (0.15466)	0.38140 (0.38146)	
	$\Delta\text{vol} = 5.0\%$ [1.4%] {-1.5%}						
rh-In $_2$ O $_3$ $R\bar{3}c$	$a = b = 5.4814$ (5.5776)	In	12c	0.0000 (0.0000)	0.0000 (0.0000)	0.35720 (0.35768)	-23984.8658
	$c = 14.4998$ (14.7543)	O	18e	0.96367 (0.96200)	0.33333 (0.33333)	0.58330 (0.58333)	(-23984.8742)
	$\Delta\text{vol} = 5.4\%$ [1.7%] {-1.4%}						
o-In $_2$ O $_3$ $Pbcn$	$a = 7.9295$ (8.0733)	In	8d	0.11483 (0.11556)	0.74607 (0.75272)	0.02627 (0.02951)	-23984.8543
	$b = 5.4821$ (5.5898)	O1	8d	0.85114 (0.84957)	0.61188 (0.60991)	0.09552 (0.10471)	(-23984.8652)
	$c = 5.5898$ (5.6912)	O2	4c	0.00000 (0.0000)	0.03792 (0.04276)	0.25000 (0.25000)	
	$\Delta\text{vol} = 5.5\%$ [1.9%] {-0.9%}						

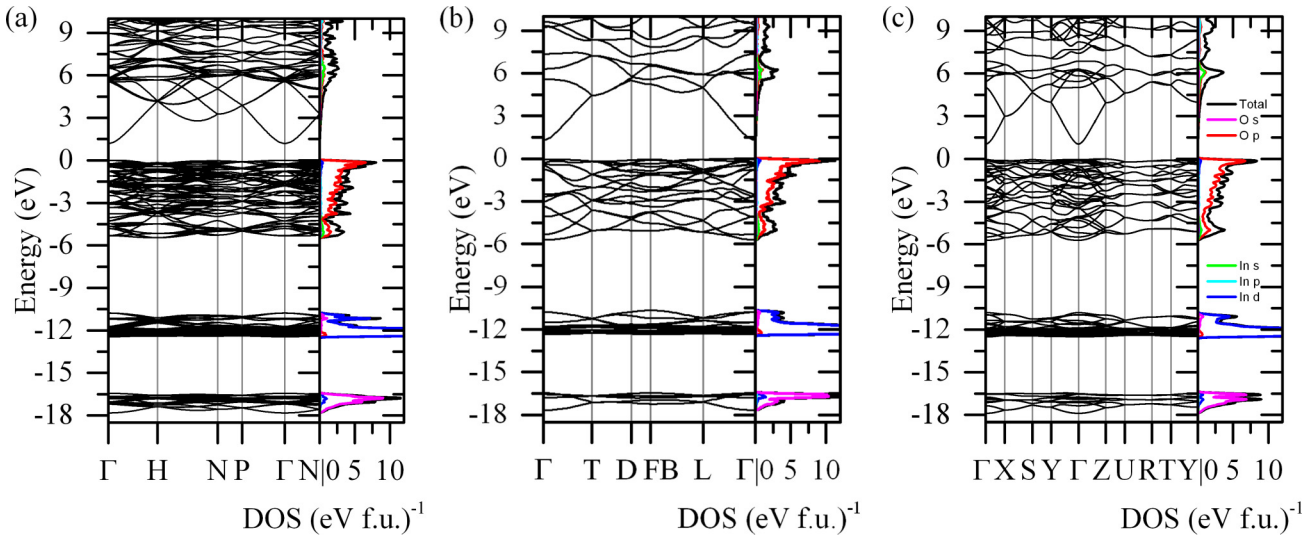


FIG. 2. Calculated band structure and PDOS diagrams for (a) *c*-, (b) *rh*-, and (c) *o*-In₂O₃. (left) The horizontal axis of the band structure panel corresponds to a path through high-symmetry points in the Brillouin zone. (right) The PDOS for O *s*, *p* and In *s*, *p*, *d* character are shown together with the total DOS per formula unit (f.u.).

ments on *c*-In₂O₃ XES and x-ray photoemission spectroscopy measurements [42–46].

B. Band gap

XAS and XES are techniques which probe the occupied and unoccupied PDOS of a material and are therefore useful in determining the band gap. However, as previously mentioned, the XAS spectra are perturbed by the presence of a core hole, and the band gap can only be determined from the XES-XAS separation once this perturbation has been accounted for. The aforementioned shifting of spectral weight to lower energies in the presence of the O 1*s* core hole can be clearly seen in each polymorph, but negligible shifts in the vicinity of the spectral weight onset are observed, so the experimentally determined band gap corresponds to the XES-XAS separation for the systems studied. The onset of spectral weight in the XES and XAS spectra is determined using peaks in the second derivative of the spectra, a technique which allows the onset to be unambiguously and reproducibly determined [47]. To

calculate the second derivative, the experimental spectra were initially smoothed using a low-pass fast Fourier transform filter to discriminate against high-frequency noise. For each polymorph, the initial XAS second-derivative peak occurred at the same energy in both the TEY and TFY spectra.

The measured and calculated band gap values are shown in Table II together with other theoretical and experimental literature values. The band gaps of the *c*-In₂O₃, *rh*-In₂O₃, and *o*-In₂O₃ polymorphs are determined to be 3.2 ± 0.3 , 3.1 ± 0.3 , and 2.9 ± 0.3 eV, respectively. For each polymorph the experimental band gaps agree with that predicted by the mBJ functional, with predicted values of 3.16, 3.26, and 2.92 eV, respectively.

Since the *o*-In₂O₃ sample is a mixture of *o*-In₂O₃, *rh*-In₂O₃, and InOOH, care must be taken in interpreting the XES-XAS separation. Considering that the Fermi energy level is expected to be uniform throughout the mixture, after accounting for differences in binding energies of the O 1*s* levels for each atomic site in the mixture and the different band gaps for each polymorph, the calculations predict that the spectral weight

TABLE II. Experimental and calculated band gaps (in eV).

	<i>c</i> -In ₂ O ₃	<i>rh</i> -In ₂ O ₃	<i>o</i> -In ₂ O ₃
E_g (expt.)	3.25 ± 0.3	3.10 ± 0.3	2.87 ± 0.3
E_g (PBE-GGA)	1.193	1.30	1.048
E_g (mBJ)	3.16	3.26	2.923
E_g (literature)	3.10^a ; 2.7 ± 0.1^b ; 2.93 ± 0.15^c ; 3.2^e ; 2.78 ± 0.04^f ; 2.7^g ; 2.83^h	3.26^a ; 3.02 ± 0.15^c	2.50^d

^aHSE03 + G₀W₀ [41].

^bExperimental result obtained using ARPES [49].

^cOptical absorption measurements [45].

^dHSE06 [51].

^eXES and XAS [46].

^fSTS[50].

^gOptical absorption measurements [48].

^hSpectroscopic ellipsometry measurements [52].

at the extrema of the XES and XAS spectra is due solely to $\text{o-In}_2\text{O}_3$, and thus the measured XES-XAS separation reflects that of $\text{o-In}_2\text{O}_3$.

The measured band gap of $\text{c-In}_2\text{O}_3$ is somewhat larger than that obtained using other techniques, being compatible within experimental error with the value of 2.93 ± 0.15 eV obtained using optical absorption measurements [45] but slightly exceeding values of 2.7, 2.7 ± 0.1 , and 2.78 ± 0.04 eV obtained using optical absorption [48], angle-resolved photoemission spectroscopy (ARPES) [49], and scanning tunneling spectroscopy (STS) [50], respectively. The reason for this disagreement may be due to the relatively slow onset of the spectral weight in the XAS spectra associated with the slow onset of states in the conduction band, shown in Fig. 2, making identifying the onset of spectral weight from the second derivative challenging. The band gap of $\text{rh-In}_2\text{O}_3$ is compatible with the results of optical measurements [45], while the measured band gap of $\text{o-In}_2\text{O}_3$ exceeds that predicted by the Heyd-Scuseria-Ernzerhof (HSE) hybrid density functional [51].

Having addressed the band gap, we now consider the electronic band structure. The PBE-GGA-calculated band structures are shown in Fig. 2. For each polymorph, the lowermost conduction bands are dispersive and have minima at the Γ point. The bands in the vicinity of the valence-band maximum (VBM) are dense and very dispersive, leading to a large peak in the initial DOS, as shown in Fig. 2. The band gaps for each polymorph are predicted to be indirect with a direct gap at the Γ points for each polymorph within 50 meV of the global VBM. For $\text{c-In}_2\text{O}_3$, theoretical work has suggested both direct [44,45,53,54] and indirect [40,41] band gaps, although all of these calculations predict that for $\text{c-In}_2\text{O}_3$ the VBM at the Γ point is within 50 meV of the global VBM, in agreement with the current work.

RIXS, a technique in which emission spectra are collected at various above-threshold excitation energies, can provide insight into the nature of the band gap. By collecting RIXS spectra as well as non-resonant XES spectra (NXES) from excitations far above the absorption threshold, the RIXS spectra can be decomposed into k -selective (“coherent”) and k -unselective (“incoherent”) contributions by subtracting the largest possible fraction of NXES spectra from the RIXS spectra as long as the remaining spectrum is positive [55]. This allows for the clarification of whether a band gap is direct or indirect independent of any theoretical input and can also allow for band mapping. In direct band gap semiconductors, such as hexagonal GaN, enhancement at the highest emission energies of the RIXS spectrum is observed, whereas for indirect band gap semiconductors, such as AlN, RIXS enhancement at lower emission energies is observed.

Several RIXS spectra for each In_2O_3 polymorph were collected in the vicinity of the absorption threshold, but upon decomposition the coherent component was indistinguishable from the NXES spectra. A representative example of the measured RIXS spectra and the extracted coherent component is shown for the case of $\text{rh-In}_2\text{O}_3$ in Fig. 3. The similarity of the coherent and incoherent components suggests that within the experimental resolution, the DOS times a dipole transition matrix element is uniform in the k space near the Γ point, which is compatible with the presence of many dispersive bands in

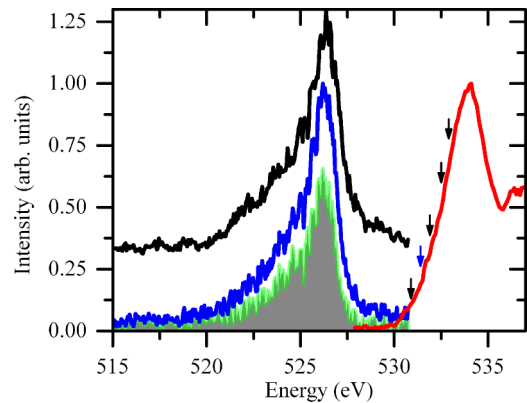


FIG. 3. Resonant and nonresonant O K -edge emission spectra of $\text{rh-In}_2\text{O}_3$ excited at 531.4 eV and far above the excitation threshold spectra are shown by blue and black lines, respectively. The coherent fraction of the blue RIXS spectrum is shown in green and is experimentally indistinguishable from the nonresonant spectrum. RIXS spectra were collected at several excitation energies, indicated by arrows on the $\text{rh-In}_2\text{O}_3$ TFY XAS spectrum. Only the blue arrow’s excitation energy is shown.

the VB, as shown in Fig. 3. Given this limitation, RIXS yields little insight into the directness of the band gap.

The indistinguishability of the RIXS spectra is in agreement with a prior study of thin films of $\text{c-In}_2\text{O}_3$ [44] in which the similarity of the coherent and incoherent components of the RIXS spectra was attributed to a direct band gap, but in our view the experimental data are inconclusive on this point. Alternative techniques such as ARPES and optical transmission measurements suggest direct and indirect band gaps for $\text{c-In}_2\text{O}_3$, respectively [48,49].

C. Density of states

The calculated density of states for each In_2O_3 polymorph is shown in Fig. 2. The valence band for each polymorph consists of three valence bands (VB1, VB2, VB3 in descending energy). Near the VBM the valence band for each polymorph has a very sharp onset corresponding to the aforementioned shallow dispersion near the VBM. VB1 is dominated by O p states, with a small admixture of In d states, with increasing contributions from In s states at the low end of the valence band. The calculated band width of VB1 (5.52, 5.78, and 5.83 eV for c- , rh- , and $\text{o-In}_2\text{O}_3$, respectively) increases with polymorph density. The fraction of spectral weight in VB1 attributed to In and O is fairly constant across polymorphs, with In contributing 13% of the spectral weight in each case. Prior work on $\text{c-In}_2\text{O}_3$ using semiempirical SICs showed that for $\text{c-In}_2\text{O}_3$ the composition of VB1 is relatively insensitive to the effect of the SICs, which do significantly affect the energetic position and fractional orbital and atomic contribution to VB2 and VB3. This explains the overall agreement between the calculated and measured spectra for $\text{c-In}_2\text{O}_3$, and the agreement for $\text{rh-In}_2\text{O}_3$ and $\text{o-In}_2\text{O}_3$ suggests that the spectral weight distribution in VB1 would be similarly unaffected by using a more sophisticated level of theory.

TABLE III. Effective mass of carriers in the conduction band evaluated at the Γ point in units of electron rest mass. Values in parentheses are experimental ARPES values [49]. Values in square brackets are calculated using the LDA functional [16].

c-In ₂ O ₃	rh-In ₂ O ₃	o-In ₂ O ₃
$\Gamma \rightarrow H$: 0.20 [0.23]	$\Gamma \rightarrow T$: 0.19	$\Gamma \rightarrow X$: 0.16
$\Gamma \rightarrow P$: 0.19 (0.18 \pm 0.02) [0.23]	$\Gamma \rightarrow L$: 0.18	$\Gamma \rightarrow Y$: 0.17
$\Gamma \rightarrow N$: 0.18 (0.24 \pm 0.02) [0.20]		$\Gamma \rightarrow Z$: 0.17

Electron effective masses

An important parameter affecting the performance of devices which may use new In₂O₃ polymorphs is the effective mass of carriers in the conduction band, which can be easily extracted from the data in Fig. 2 by fitting a polynomial to the E vs k mesh between the two high-symmetry k points and evaluating the effective mass at the Γ point:

$$\frac{1}{m_{e^*}} = \frac{1}{\hbar^2} \left. \frac{\partial^2 E(\vec{k})}{\partial \vec{k}^2} \right|_{\vec{k}=\Gamma},$$

where m_{e^*} is the effective electronic mass. The calculated effective electron mass for different polymorphs as a fraction of the free-electron rest mass is shown in Table III. The calculated effective mass in c-In₂O₃ is fairly isotropic and is estimated to be between $0.18m_e$ and $0.20m_e$, depending on the direction, where m_e is the electronic rest mass, in general agreement with the results obtained using the LDA [16] and HSE03 functionals [41]. Similar values are obtained for rh-In₂O₃. In contrast, the effective mass of o-In₂O₃ is expected to be between $0.16m_e$ and $0.17m_e$, 12% smaller than that of c- and rh-In₂O₃. The calculated values for c-In₂O₃ are in general agreement with values obtained using a variety of experimental techniques. Effective masses between $0.18m_e \pm 0.02m_e$ and $0.24m_e \pm 0.02m_e$ have been obtained using ARPES [49,56], while spectroscopic ellipsometry [57] and Hall mobility and Seebeck coefficient measurements [58] suggest a value of $0.30m_e$. This similarity of m_{e^*} between polymorphs is in agreement with prior work on transition- and posttransition-metal oxides, which shows that the effective mass is relatively unchanged for polymorphs of single-cation oxides even in cases where the oxygen atoms have different coordination [16,59]. The oxygen atoms in the polymorphs studied in this work are all tetrahedrally coordinated, with local structural differences being due to changes in corner, edge, and face sharing between [InO₆] octahedra.

The optical band gap of c-In₂O₃ exceeds that of the fundamental band gap since transitions from the valence to

conduction bands are dipole forbidden due to the crystal symmetry, leading to an experimental effective optical band gap 0.62 eV greater than the fundamental band gap [45,54], in agreement with a 0.7 eV shift calculated in this work. Using a hybrid functional, a similar 0.6 eV increase of the effective optical band gap has been predicted for o-In₂O₃, despite the absence of a center of inversion (a 0.4 eV increase is predicted in this study) [51]. The band gap of 2.9 ± 0.3 eV of o-In₂O₃ measured in this study suggests an effective optical band gap of 3.5 ± 0.3 eV, similar to the 3.55 eV effective optical band gap of c-In₂O₃ [45]. Given the significant usage of c-In₂O₃ in applications which require both optical transparency and good conductivity, the similar effective optical band gaps of c- and o-In₂O₃ coupled with the lower m_{e^*} of carriers in o-In₂O₃ suggest that substituting c-In₂O₃ with o-In₂O₃ in these applications could result in devices with improved energy efficiency.

D. Conclusion

The electronic structure of the new orthorhombic In₂O₃ polymorph together with the cubic bixbyite and rhombohedral In₂O₃ polymorphs has been studied experimentally and theoretically. Excellent overall agreement between the measured and calculated spectra is obtained, providing experimental support for the calculated electronic structure. The band gap of o-In₂O₃ has been identified as 2.9 ± 0.3 eV, in agreement with a calculated value of 2.92 eV, representing the first measurement of this important parameter. The effective mass of carriers near the conduction-band edge is predicted to be isotropic and 12% smaller than that of c-In₂O₃ with $m_{e^*} = 0.17m_e$ but with a similar effective optical band gap. Given the potential benefits to current applications, this suggests that further work to obtain single-phase o-In₂O₃ is warranted.

ACKNOWLEDGEMENTS

Research described in this work was performed at the Canadian Light Source, which is supported by the Natural Sciences and Engineering Research Council of Canada (NSERC), the National Research Council Canada, the Canadian Institutes of Health Research, the Province of Saskatchewan, Western Economic Diversification Canada, and the University of Saskatchewan. The Advanced Light Source is supported by the Director, Office of Science, Office of Basic Energy Sciences, of the U.S. Department of Energy under Contract No. DE-AC02-05CH11231. We acknowledge support from NSERC and the Canada Research Chair program. The computational component of this work was enabled by resources provided by WestGrid (www.westgrid.ca) and Compute Canada Calcul Canada (www.computecanada.ca).

[1] O. Bierwagen, *Semicond. Sci. Technol.* **30**, 024001 (2015).

[2] C. G. Granqvist, *Appl. Phys. A* **57**, 19 (1993).

[3] A. N. Tiwari, G. Khrypunov, F. Kurdzesau, D. L. Bätzner, A. Romeo, and H. Zogg, *Prog. Photovoltaics* **12**, 33 (2004).

[4] G. Gu, V. Bulović, P. E. Burrows, S. R. Forrest, and M. E. Thompson, *Appl. Phys. Lett.* **68**, 2606 (1996).

[5] A. Porch, D. V. Morgan, R. M. Perks, M. O. Jones, and P. P. Edwards, *J. Appl. Phys.* **96**, 4211 (2004).

[6] G. S. Chae, *Jpn. J. Appl. Phys.* **40**, 1282 (2001).

[7] M. T. Hardy, C. O. Holder, D. F. Feezell, S. Nakamura, J. S. Speck, D. A. Cohen, and S. P. Denbaars, *Appl. Phys. Lett.* **103**, 081103 (2013).

- [8] A. Pourhashemi, R. M. Farrell, D. A. Cohen, J. S. Speck, S. P. DenBaars, and S. Nakamura, *Appl. Phys. Lett.* **106**, 111105 (2015).
- [9] T. Takada, K. Suzuki, and M. Nakane, *Sens. Actuators, B* **13**, 404 (1993).
- [10] S. Sänze, A. Gurlo, and C. Hess, *Angew. Chem., Int. Ed.* **52**, 3607 (2013).
- [11] M. Pashchanka, R. C. Hoffmann, A. Gurlo, and J. J. Schneider, *J. Mater. Chem.* **20**, 8311 (2010).
- [12] A. Oprea, A. Gurlo, N. Bârsan, and U. Weimar, *Sens. Actuators, B* **139**, 322 (2009).
- [13] A. Gurlo, N. Bârsan, M. Ivanovskaya, U. Weimar, and W. Göpel, *Sens. Actuators, B* **47**, 92 (1998).
- [14] J. E. Koo, S. T. Lee, and J. H. Chang, *J. Nanosci. Nanotechnol.* **15**, 669 (2015).
- [15] R. Caracas and R. E. Cohen, *Phys. Rev. B* **76**, 184101 (2007).
- [16] S. Z. Karazhanov, P. Ravindran, P. Vajeeston, A. Ulyashin, T. G. Finstad, and H. Fjellvåg, *Phys. Rev. B* **76**, 075129 (2007).
- [17] A. Gurlo, P. Kroll, and R. Riedel, *Chem. Eur. J.* **14**, 3306 (2008).
- [18] A. Walsh, C. R. Catlow, A. A. Sokol, and S. M. Woodley, *Chem. Mater.* **21**, 4962 (2009).
- [19] M. F. Bekheet, M. R. Schwarz, S. Lauterbach, H.-J. Kleebe, P. Kroll, R. Riedel, and A. Gurlo, *Angew. Chem., Int. Ed.* **52**, 6531 (2013).
- [20] B. García-Domene, J. A. Sans, O. Gomis, F. J. Manjón, H. M. Ortiz, D. Errandonea, D. Santamaría-Pérez, D. Martínez-García, R. Vilaplana, A. L. J. Pereira, A. Morales-García, P. Rodríguez-Hernández, A. Muñoz, C. Popescu, and A. Segura, *J. Phys. Chem. C* **118**, 20545 (2014).
- [21] R. D. Shannon, *Solid State Commun.* **4**, 629 (1966).
- [22] A. Malik, R. Nunes, and R. Martins, *MRS Proceedings* **481**, 599 (1997).
- [23] M. Epifani, P. Siciliano, A. Gurlo, N. Barsan, and U. Weimar, *J. Am. Chem. Soc.* **126**, 4078 (2004).
- [24] C. Y. Wang, V. Cimalla, H. Romanus, T. Kups, G. Ecke, T. Stauden, M. Ali, V. Lebedev, J. Pezoldt, and O. Ambacher, *Appl. Phys. Lett.* **89**, 011904 (2006).
- [25] A. Gurlo, S. Lauterbach, G. Miehe, H. J. Kleebe, and R. Riedel, *J. Phys. Chem. C* **112**, 9209 (2008).
- [26] C. H. Lee, M. Kim, T. Kim, A. Kim, J. Paek, J. W. Lee, S. Y. Choi, K. Kim, J. B. Park, and K. Lee, *J. Am. Chem. Soc.* **128**, 9326 (2006).
- [27] J. Q. Xu, Y. P. Chen, Q. Y. Pan, Q. Xiang, Z. X. Cheng, and X. W. Dong, *Nanotechnology* **18**, 115615 (2007).
- [28] H. Jiang, L. Zhao, L. Gai, L. Ma, Y. Ma, and M. Li, *CrystEngComm* **15**, 7003 (2013).
- [29] D. Liu, W. Lei, S. Qin, L. Hou, Z. Liu, Q. Cui, and Y. Chen, *J. Mater. Chem. A* **1**, 5274 (2013).
- [30] J. Yin and H. Cao, *Inorg. Chem.* **51**, 6529 (2012).
- [31] A. Gurlo, D. Dzivenko, P. Kroll, and R. Riedel, *Phys. Status Solidi RRL* **2**, 269 (2008).
- [32] K. Schwarz, P. Blaha, and G. Madsen, *Comput. Phys. Commun.* **147**, 71 (2002).
- [33] F. Tran and P. Blaha, *Phys. Rev. Lett.* **102**, 226401 (2009).
- [34] J. P. Perdew, A. Ruzsinszky, G. I. Csonka, O. A. Vydrov, G. E. Scuseria, L. A. Constantin, X. Zhou, and K. Burke, *Phys. Rev. Lett.* **100**, 136406 (2008).
- [35] J. P. Perdew and Y. Wang, *Phys. Rev. B* **45**, 13244 (1992).
- [36] K. Schwarz, A. Neckel, and J. Nordgren, *J. Phys. F* **9**, 2509 (1979).
- [37] G. Mahan, *Phys. Rev. B* **21**, 1421 (1980).
- [38] U. von Barth and G. Grossmann, *Phys. Rev. B* **25**, 5150 (1982).
- [39] M. Marezio, *Acta Crystallogr.* **20**, 723 (1966).
- [40] P. Erhart, A. Klein, R. G. Egdell, and K. Albe, *Phys. Rev. B* **75**, 153205 (2007).
- [41] F. Fuchs and F. Bechstedt, *Phys. Rev. B* **77**, 155107 (2008).
- [42] A. Klein, *Appl. Phys. Lett.* **77**, 2009 (2000).
- [43] C. McGuinness, C. B. Stagescu, P. J. Ryan, J. E. Downes, D. Fu, K. E. Smith, and R. G. Egdell, *Phys. Rev. B* **68**, 165104 (2003).
- [44] L. F. J. Piper, A. DeMasi, S. W. Cho, K. E. Smith, F. Fuchs, F. Bechstedt, C. Körber, A. Klein, D. J. Payne, and R. G. Egdell, *Appl. Phys. Lett.* **94**, 022105 (2009).
- [45] P. D. C. King, T. D. Veal, F. Fuchs, C. Y. Wang, D. J. Payne, A. Bourlange, H. Zhang, G. R. Bell, V. Cimalla, O. Ambacher, R. G. Egdell, F. Bechstedt, and C. F. McConville, *Phys. Rev. B* **79**, 205211 (2009).
- [46] J. A. McLeod, N. A. Skorikov, L. D. Finkelstein, E. Z. Kurmaev, and A. Moewes, *J. Phys. Chem. C* **116**, 24248 (2012).
- [47] E. Z. Kurmaev, R. G. Wilks, A. Moewes, L. D. Finkelstein, S. N. Shamin, and J. Kuneš, *Phys. Rev. B* **77**, 165127 (2008).
- [48] K. Irmscher, M. Naumann, M. Pietsch, Z. Galazka, R. Uecker, T. Schulz, R. Schewski, M. Albrecht, and R. Fornari, *Phys. Status Solidi A* **211**, 54 (2014).
- [49] V. Scherer, C. Janowitz, A. Krapf, H. Dwelk, D. Braun, and R. Manzke, *Appl. Phys. Lett.* **100**, 212108 (2012).
- [50] D. Braun, V. Scherer, C. Janowitz, Z. Galazka, R. Fornari, and R. Manzke, *Phys. Status Solidi A* **211**, 59 (2014).
- [51] A. Walsh and D. O. Scanlon, *Phys. Rev. B* **88**, 161201 (2013).
- [52] R. Schmidt-Grund, H. Krauß, C. Kranert, M. Bonholzer, and M. Grundmann, *Appl. Phys. Lett.* **105**, 111906 (2014).
- [53] O. N. Mryasov and A. J. Freeman, *Phys. Rev. B* **64**, 233111 (2001).
- [54] A. Walsh, J. L. F. Da Silva, S.-H. Wei, C. Körber, A. Klein, L. F. J. Piper, A. DeMasi, K. E. Smith, G. Panaccione, P. Torelli, D. J. Payne, A. Bourlange, and R. G. Egdell, *Phys. Rev. Lett.* **100**, 167402 (2008).
- [55] S. Eisebitt and W. Eberhardt, *J. Electron Spectrosc. Relat. Phenom.* **110-111**, 335 (2000).
- [56] K. H. L. Zhang, R. G. Egdell, F. Offi, S. Iacobucci, L. Petaccia, S. Gorovikov, and P. D. C. King, *Phys. Rev. Lett.* **110**, 056803 (2013).
- [57] H. Fujiwara and M. Kondo, *Phys. Rev. B* **71**, 075109 (2005).
- [58] N. Preissler, O. Bierwagen, A. T. Ramu, and J. S. Speck, *Phys. Rev. B* **88**, 085305 (2013).
- [59] J. E. Medvedeva and C. L. Hettiarachchi, *Phys. Rev. B* **81**, 125116 (2010).